The Astrophysical Journal, 983:141 (9pp), 2025 April 20 https://doi.org/10.3847/1538-4357/adc2fe


# Redshift Evolution of the X-Ray and Ultraviolet Luminosity Relation of Quasars: Calibrated Results from SNe Ia

Xiaolei Li[1], Ryan E. Keeley[2], and Arman Shafieloo[3,4]
[1] College of Physics, Hebei Normal University, Shijiazhuang 050024, People's Republic of China; lixiaolei@hebtu.edu
[2] Department of Physics, University of California Merced, 5200 North Lake Road, Merced, CA 95343, USA; rkeeley@ucmerced.edu
[3] Korea Astronomy and Space Science Institute, Daejeon 34055, Republic of Korea; shafieloo@kasi.re.kr
[4] University of Science and Technology, Yuseong-gu 217 Gajeong-ro, Daejeon 34113, Republic of Korea
*Received 2024 September 6; revised 2025 March 14; accepted 2025 March 18; published 2025 April 16*

## Abstract

Quasars could serve as standard candles if the relation between their ultraviolet (UV) and X-ray luminosities can be accurately calibrated. Previously, we developed a model-independent method to calibrate quasar standard candles using the distance–redshift relation reconstructed from Type Ia supernovae (SNe Ia) at $z < 2$ using Gaussian process regression. Interestingly, we found that the calibrated quasar standard candle data set preferred a deviation from ΛCDM at redshifts above $z > 2$. One possible interpretation of these findings is that the calibration parameters of the quasar UV and X-ray luminosity relationship evolves with redshift. In order to test the redshift dependence of the quasar calibration in a model-independent manner, we divided the quasar sample whose redshift overlaps with the redshift coverage of Pantheon+ SNe Ia compilation into two subsamples: a low-redshift quasar subsample and a high-redshift quasar subsample. Assuming all the quasar samples are reliable, our results show that there is about a $4\sigma$ inconsistency between the quasar parameters inferred from the subsamples without considering evolution. This inconsistency suggests the possibility of considering redshift evolution for the relationship between the quasars' UV and X-ray luminosities. We then test an explicit parameterization of the redshift evolution of the quasar calibration parameters via $\gamma(z) = \gamma_0 + \gamma_1(1+z)$ and $\beta(z) = \beta_0 + \beta_1(1+z)$. Combining this redshift-dependent calibration relationship with the distance–redshift relationship reconstructed from the Pantheon+ supernova compilation, we find the high-redshift subsample and low-redshift subsample become consistent at the $2\sigma$ level, which means that the parameterized form of $\gamma(z)$ and $\beta(z)$ works well at describing the evolution of the quasar calibration parameters.

*Unified Astronomy Thesaurus concepts:* Observational cosmology (1146); Gaussian Processes regression (1930); Quasars (1319)

## 1. Introduction

Because quasars are among the most luminous persistent sources in the Universe, they can be detected out to redshifts $z \sim 7$ (D. J. Mortlock et al. 2011; E. Banados et al. 2018; F. Wang et al. 2021). Thus, if quasars can be used as standard candles, then they can measure the expansion rate of the Universe beyond the redshifts probed by Type Ia supernovae (SNe Ia) and help us to better understand dark energy. The standard cosmological scenario, the so-called Lambda cold dark matter (ΛCDM) model, accurately describes the physics of the early Universe, the formation of large-scale structure, and the late-time acceleration of the Universe. However, this model suffers from some profound theoretical difficulties, including the fine-tuning problem and the coincidence problem, as well as observational tensions including the Hubble tension and S8 tension (S. Weinberg 1989; S. M. Carroll et al. 1992; A. D. Dolgov 1997; J. Martin 2012; A. G. Riess et al. 2019; Planck Collaboration et al. 2020; E. Di Valentino et al. 2021).

Historically, there have been a number of attempts to use quasars as standard candles from a variety of emission features. For example, J. A. Baldwin (1977) showed that the width of quasars' emission lines was correlated with their luminosity, thus demonstrating an avenue by which quasars could be standard candles; however, in P. S. Osmer & J. C. Shields (1999), the authors argued that the "substantial scatter" in this relationship makes it not useful for cosmology. Furthermore, in J. M. Wang et al. (2013), the authors demonstrated that super-Eddington accreting massive black holes have a luminosity determined by the mass of the black hole and thus that these objects are standard candles. F. La Franca et al. (2014) showed that the X-ray variability of quasars can be used to measure their luminosities, and in the work of D. Watson et al. (2011), F. Melia (2014), and E. Kilerci Eser et al. (2015), the authors show that the radius of a quasar can be used to measure its luminosity.

Despite these multiple avenues by which quasars could serve as standard candles, the observed relationship between the log of the X-ray and ultraviolet (UV) luminosities (H. Tananbaum et al. 1979; G. Zamorani et al. 1981; Y. Avni & H. Tananbaum 1986; E. Lusso et al. 2010; F. Vagnetti et al. 2010) has recently been widely used to measure cosmological distances (G. Risaliti & E. Lusso 2015, 2017; E. Lusso & G. Risaliti 2017; G. Risaliti & E. Lusso 2019; N. Khadka & B. Ratra 2020, 2021; E. Lusso et al. 2020).

Initially, this data set of quasar fluxes was found to fit the ΛCDM model well and matched the distances inferred from SNe Ia (G. Risaliti & E. Lusso 2015). However, various groups found that there exists a deviation between the ΛCDM model and the quasar distances when they are calibrated with such a linear relationship (G. Risaliti & E. Lusso 2019; N. Khadka & B. Ratra 2021; X. Li et al. 2021). For instance, G. Risaliti &

E. Lusso (2019) found that the best-fit value of the present matter density ($\Omega_{m,0}$) is different if constrained with only high-redshift quasars or only low-redshift quasars. Furthermore, N. Khadka & B. Ratra (2021) found that the inferred quasar calibration parameters depend on which cosmological distance is used, concluding that only quasars in the range $z < 1.5$–$1.7$ are reliable probes of cosmological distances. Also, X. Li et al. (2021) found that a model-independent calibration of quasars can be performed out to $z < 2$, and that calibrated quasar data set deviated from ΛCDM at $z > 2$. In A. Sacchi et al. (2022), the authors performed a one-by-one analysis of a sample of 130 quasars at $z > 2.5$ with high-quality X-ray and UV spectroscopic observations. The results show that the X-ray–UV calibration still holds at $z > 2.5$. On the other hand, in the work of Z. Li et al. (2022), the authors combined the Parameterization based on cosmic Age (PAge) approximation and a high-quality quasar sample to search for the origins of the deviation and found that the deviation from the standard ΛCDM model probably originates from the redshift-evolution effects and nonuniversal intrinsic dispersion of the quasar luminosity relation rather than new cosmological physics. Moreover, in B. Wang et al. (2022), the authors constructed a three-dimensional and redshift–evolutionary X-ray and UV luminosity relation for quasars from the powerful statistic tool called Copula and found that the constructed $L_X - L_{UV}$ relation from Copula is more viable, and the observations favored their modified X-ray and UV luminosity relation with the additional redshift-dependent term. Their results confirmed that the quasars can be regarded as a reliable indicator of the cosmic distance if the $L_X$–$L_{UV}$ relation from Copula is used to calibrate quasar data. In a recent work, B. Wang et al. (2024) compare three different quasar $L_X$–$L_{UV}$ relations (two $L_X$–$L_{UV}$ relations include no redshift–evolutionary relation, while two $L_X$–$L_{UV}$ relations allow for redshift evolution) and conclude that the $L_X$–$L_{UV}$ relations that allow for redshift evolution are favored by the observations. By dividing the quasar sample into a low-redshift subsample and a high-redshift subsample, the constraint results on PAge parameters are consistent for the redshift–evolutionary relation, while the constraint results about quasar parameters, i.e., $\gamma$ and $\beta$, are still in tension.

These works collectively indicate that there is some tension between the quasar data and the joint model, including both the standard UV and X-ray luminosity relationship and the ΛCDM model. This tension could either be explained by extending the cosmological model beyond ΛCDM or by adding a redshift evolution to the quasar calibration parameters.

Different methods have been used in the literature to calibrate quasar distances. For instance, G. Risaliti & E. Lusso (2015) use narrow redshift bins of quasars to estimate $\gamma$ in that narrow redshift bin and then use the average value of $\gamma$ over the redshift bins to calculate cosmological constraints. Also, E. Lusso et al. (2020) fit the luminosity distance with a fifth-grade polynomial in $\log(1+z)$ in order to calibrate quasar UV and X-ray luminosity relation. In this work, we follow the method developed in X. Li et al. (2021), where the quasar UV and X-ray luminosity relationship is calibrated in a cosmological-model-independent manner. This is achieved by using Gaussian process (GP) regression to reconstruct the distance–redshift relationship from SNe Ia and then varying the quasar calibration parameters such that these reconstructions are maximally consistent with the quasar data. We use this methodology to test if different high-redshift and low-redshift subsamples of the quasar data are consistent with each other. We also use this methodology to test a new quasar calibration parameterization that evolves with redshift, thus accounting for the tension between high-redshift and low-redshift subsets of the quasar data set.

## 2. Calibration Method and Quasar Sample

The standard relationship between quasars' X-ray and UV luminosities is parameterized as

$$\log(L_X) = \gamma \log(L_{UV}) + \beta, \tag{1}$$

where $\gamma$ and $\beta$ are the two quasar calibration parameters that are fit to the data and $\log \equiv \log_{10}$. With the relation between the luminosity $L$ and the flux $F$, $L = 4\pi D_L^2 F$, we can rewrite Equation (1) as

$$\log(F_X) = \gamma \log(F_{UV}) + (2\gamma - 2)\log(D_L) + (\gamma - 1)\log(4\pi) + \beta, \tag{2}$$

where $F_{UV}$ and $F_X$ are the fluxes measured at fixed rest-frame wavelengths and $D_L$ is the luminosity distance. From this relation, we can see that the quasar calibration parameters are degenerate with the cosmological distances. Thus, any observed deviation in the data could potentially be explained by either extending the cosmological model or by extending the quasar calibration relation. In keeping with the theme of developing statistical methods to make joint cosmological constraints from a variety of data sets, we use the distances from SNe Ia and investigate whether an extension in the quasar calibration relation is needed by the data. This is, in essence, why we find extending the calibration model more convincing than extending the cosmological model; extending the cosmological model to explain this tension in the quasar data would be inconsistent with the results from SNe Ia. This also highlights the importance of model-independent methods; we are as flexible and as agnostic, with regards to the true cosmology, as the data allow.

Following the work of X. Li et al. (2021), we use cosmological distances from SNe Ia to break the degeneracy between the quasar calibration parameters and cosmological distances and thus constrain the quasar calibration parameters. We generate 1000 realizations of the unanchored luminosity distance $D_L H_0$ from the posterior of the Pantheon+ compilation from D. Scolnic et al. (2022) calculated with GP regression. It is worth noting that the GP reconstruction is weakly dependent on the chosen mean function, especially in regions that the data do not constrain well. Different mean functions will cause the data to prefer different regions of the hyperparameter space, which can effect the uncertainty in the reconstruction where the data do not constrain it well. For comprehensive details on this sampling method, we refer the readers to K. Liao et al. (2019, 2020), and for an extensive discourse on GP regression, please refer to C. E. Rasmussen & C. K. I. Williams (2006), T. Holsclaw et al. (2010, 2011), A. Shafieloo et al. (2012), S. Joudaki et al. (2018), and S.-g. Hwang et al. (2023). We then calculate the predicted quasar X-ray flux ($F_X^{pre}$) corresponding to these unanchored luminosity distances $D_L H_0$, along with the parameters of the standard quasar calibration relation, by rewriting

Equation (2) as

$$\log(F_{\rm X}^{\rm pre}) = \gamma\log(F_{\rm UV}) + (2\gamma - 2)\log(D_{\rm L}H_0) - (2\gamma - 2)\log(H_0) + (\gamma - 1)\log(4\pi) + \beta. \quad (3)$$

This allows us to compare the observed values of the quasars' X-ray flux $\log(F_{\rm X})$ and the values predicted by the quasar calibration parameters and cosmological parameters.

Then, following G. Risaliti & E. Lusso (2015) and E. Lusso et al. (2020), we define the likelihood ($\mathcal{L} = \exp(-\chi^2/2)$) of the quasar parameters based on a modified $\chi^2$ function, which includes a penalty term for the intrinsic dispersion $\delta$,

$$\chi^2 = \sum_i \left[ \frac{(\log(F_{\rm X}(\gamma, \beta, H_0))_i^{\rm pre} - \log(F_{\rm X})_i^{\rm obs})^2}{s_i^2} + \ln(s_i^2) \right], \quad (4)$$

where $s_i^2 = \sigma^2_{\log(F_{\rm X})} + \gamma^2\sigma^2_{\log(F_{\rm UV})} + \delta^2$. The intrinsic dispersion $\delta$ is considered in order to allow for scatter in the $L_{\rm X}$–$L_{\rm UV}$ relation beyond any measurement noise (G. Risaliti & E. Lusso 2019; E. Lusso et al. 2020).

When calibrating the standard quasar calibration relation, $L_{\rm X}$–$L_{\rm UV}$, there is a total of four free parameters that need to be constrained, i.e., the slope $\gamma$, the intercept $\beta$, and the intrinsic dispersion parameter $\delta$, as well as the Hubble constant $H_0$, as seen in Equations (3) and (4).

In addition, we also consider the case where the quasar calibration parameters, $\gamma$ and $\beta$, can evolve with redshift as $\gamma(z) = \gamma_0 + \gamma_1 \times (1+z)$ and $\beta(z) = \beta_0 + \beta_1 \times (1+z)$, respectively. By considering the redshift evolution of the quasar calibration parameters, we now have six parameters, i.e., $\gamma_0$, $\gamma_1$, $\beta_0$, $\beta_1$, $\delta$, and $H_0$, to be constrained.

The statistical analysis is performed by using the Markov Chain Monte Carlo method as implemented in the Python package `emcee` (D. Foreman-Mackey et al. 2013), and the converged chains are analyzed with `GetDist` (A. Lewis 2019).

During our analysis, we use the 2421 quasar sample compiled in E. Lusso et al. (2020) with redshifts spanning $0.009 < z < 7.6$. In order to check the redshift dependence of the quasar parameters, we divided the quasar sample into two subsamples and do the calibration following the method described above. There are 2067 quasars in the sample whose redshift lies within the redshift range of the SNe Ia and thus can be used to do the calibration directly. We first divided the 2067 quasars sample into two similar groups: a lower half, which has 1033 quasars with $z < 1.16$ (hereafter the low-redshift subsample), and a higher half, which has 1034 quasars with $z > 1.16$ (hereafter the high-redshift subsample). Furthermore, we also calibrate the quasar parameters using all the 2067 quasars that have redshifts in the range covered by SNe Ia.

We should emphasize here that quasars at redshift lower than 0.7 may be less reliable due to some residual contamination from the host galaxy (E. Lusso et al. 2020). One can also add a filter of $z > 0.7$ to the full sample. In our analysis, we use the full sample to check the redshift dependence for the UV and X-ray luminosity relationship. However, we show the calibrated results for the sample discarding quasars at $z < 0.7$ in the Appendix. Importantly, the high-redshift subsample prefers an evolution in the quasar calibration parameters regardless of any $z < 0.7$ contamination.

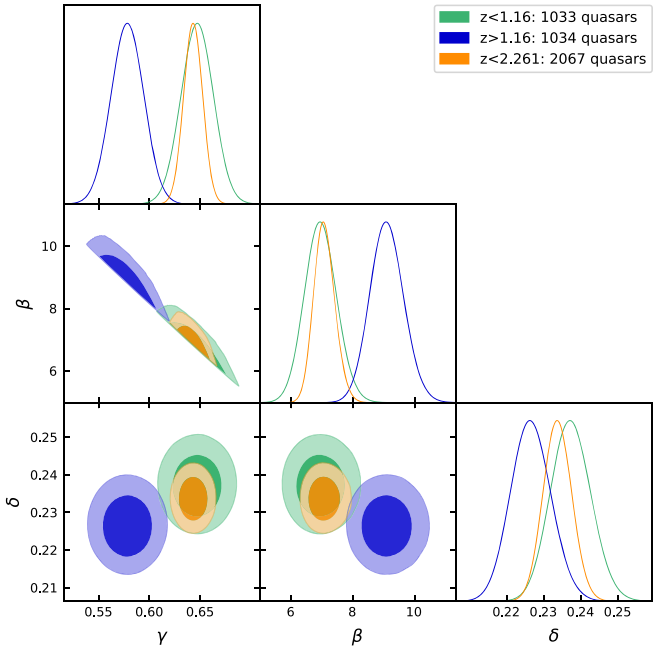


**Figure 1.** Model-independent calibration results for the quasar parameters. GP reconstructions of $D_{\rm L}H_0$ from the Pantheon+ SNe Ia compilation were used. The contours represent the $1\sigma$, $2\sigma$ uncertainties for $\gamma$, $\beta$, and $\delta$. Marginal one-dimensional distributions for each parameter are shown along the diagonal of the corner plot.

## 3. Calibration Results and Discussions

In this section, we consider two different quasar relations to test the discrepancy between the high-redshift quasar subsample and the low-redshift quasar subsample.

### 3.1. Nonevolution of Quasar Relation

Based on the method described in Section 2, we obtain the calibration results with the three quasar subsamples. The posteriors for the quasar parameters are shown in Figure 1. The green contours (lines) denote the results from the low-redshift subsample and the blue contours (lines) denote the results from the high-redshift subsample, while the orange contours (lines) show the results from the 2067 quasar samples whose redshift ranges overlap with the redshift range of SNe Ia. As we can see from Figure 1, the constraints from the 2067 quasar sample are consistent with the results from the low-redshift subsample, while both of them are in tension with the results from the high-redshift quasar subsample. We can also see a diagonal cut in the $\gamma$ and $\beta$ plane for both the high-$z$ and low-$z$ subsamples, which is mainly attributed to the prior distribution selected for $H_0$. This result suggests that the parameters $\gamma$, $\beta$ and $H_0$ are highly correlated.

The numerical results, including the median values of quasar parameters and the $1\sigma$ uncertainties, are shown in Table 1. There is about a $4\sigma$ deviation for the parameters $\gamma$ and $\beta$ between the high-redshift subsample and the low-redshift subsample. This deviation indicates that the UV and X-ray luminosity relationship for quasars may evolve with redshift. On the other hand, the calibration results for $\gamma$ from the low-redshift subsample are consistent with previous work by X. Li et al. (2021), which gave $\gamma = 0.649 \pm 0.007$. However, the calibration results for $\gamma$ from the high-redshift sample indicate $4.4\sigma$ deviation from the previous work by X. Li et al. (2021).

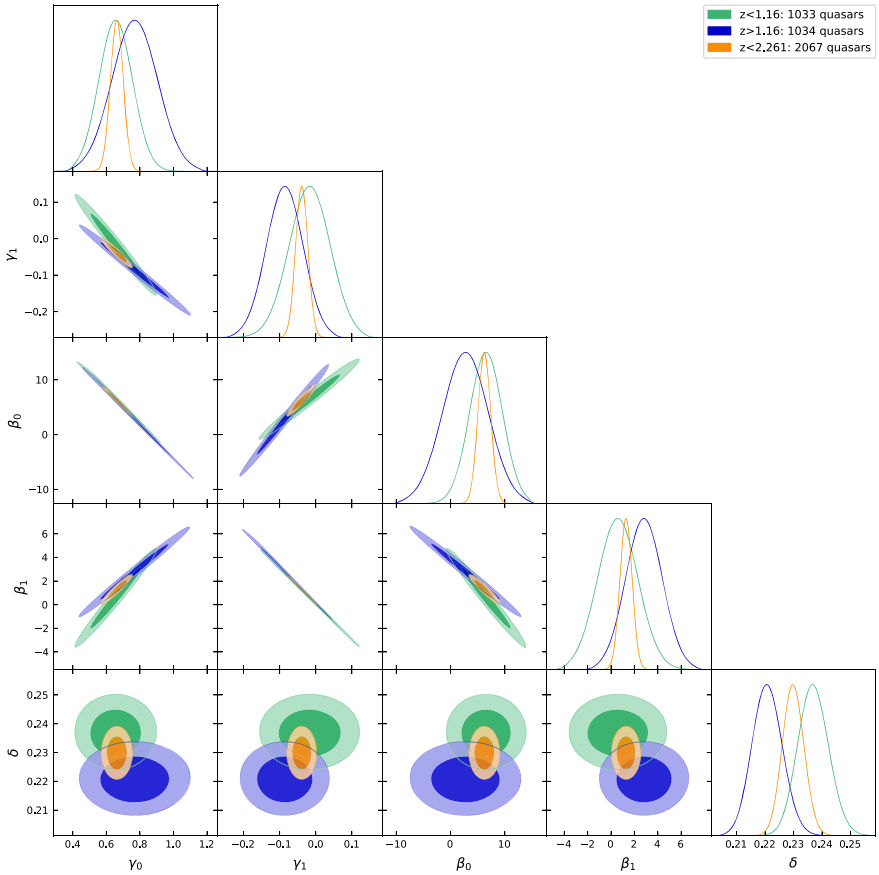


**Figure 2.** Same as Figure 1 but for the case where the quasar parameters evolve as $\gamma(z) = \gamma_0 + \gamma_1 \times (1 + z)$ and $\beta(z) = \beta_0 + \beta_1 \times (1 + z)$.

**Table 1**
The Median Values of the Quasar Parameters and Their $1\sigma$ Uncertainties as well as the $\chi^2$ from Different Quasar Subsamples for the Case where They Do Not Evolve with Redshift

| Subsamples | $\gamma$ | $\beta$ | $\delta$ | $\chi^2$ |
|---|---|---|---|---|
| $z < 1.16$: 1033 quasars | $0.647 \pm 0.016$ | $6.95 \pm 0.52$ | $0.2373 \pm 0.0054$ | $-1878.88$ |
| $z > 1.16$: 1034 quasars | $0.578 \pm 0.016$ | $9.11 \pm 0.55$ | $0.2266 \pm 0.0054$ | $-1929.61$ |
| $z < 2.26$: 2067 quasars | $0.6431 \pm 0.0092$ | $7.08^{+0.31}_{-0.36}$ | $0.2337 \pm 0.0038$ | $-3760.30$ |

**Note.** GP reconstructions of $D_L H_0$ based on the Pantheon+ SNe Ia compilation were used.

We also show the best-fit values of quasar parameters and the $\chi^2$ values in Table 2.

All the results confirm that there is a tension between the quasar calibration parameters fit at low and high redshifts. Therefore, we should allow for the quasar calibration parameters to evolve with redshift in order to accurately use quasars as standard candles.

### 3.2. Redshift Evolution of Quasar Relation

In this section, we consider the case for the UV and X-ray luminosity relationship to evolve with redshift following $\gamma = \gamma_0 + \gamma_1(1+z)$ and $\beta = \beta_0 + \beta_1(1+z)$ in Equations (1), (2), and (3). The calibration results for the quasar parameters are shown in Figure 2, and the numerical results, including the median values of quasar parameters and the $1\sigma$ uncertainties, are shown in Table 3. We also show the best-fit results for quasar parameters and accordingly $\chi^2$ in Table 4. Note that the

**Table 2**
The Best-fit Quasar Parameters for the Case where They Do Not Evolve With Redshift

| Subsamples | $\gamma$ | $\beta$ | $\delta$ | $\chi^2$ |
|---|---|---|---|---|
| $z < 1.16$: 1033 quasars | 0.645 | 7.56 | 0.2355 | $-1914.65$ |
| $z > 1.16$: 1034 quasars | 0.573 | 9.34 | 0.2256 | $-1963.84$ |
| $z < 2.26$: 2067 quasars | 0.638 | 7.11 | 0.2331 | $-3848.34$ |

**Note.** GP reconstructions of $D_L H_0$ based on the Pantheon+ SNe Ia compilation were used.

$\chi^2$ values listed in these tables include the $\sum_i \ln s_i$ penalty term as in Equation (4) and so have negative values.

As we can see from Figure 2, the results for the quasar calibration parameters from the low-redshift subsample and the high-redshift subsample are consistent at the $2\sigma$ level, which indicates that the parametric form for $\gamma$ and $\beta$ works well in

**Table 3**
As Table 1 but for the Case where Quasar Parameters Do Evolve with Redshift as $\gamma(z) = \gamma_0 + \gamma_1 \times (1 + z)$ and $\beta(z) = \beta_0 + \beta_1 \times (1 + z)$

| Subsamples | $\gamma_0$ | $\gamma_1$ | $\beta_0$ | $\beta_1$ | $\delta$ | $\chi^2$ |
|---|---|---|---|---|---|---|
| $z < 1.16$: 1033 quasars | $0.656 \pm 0.099$ | $-0.017 \pm 0.057$ | $6.5 \pm 3.0$ | $0.6 \pm 1.7$ | $0.2370 \pm 0.0054$ | −1904.50 |
| $z > 1.16$: 1034 quasars | $0.770 \pm 0.130$ | $-0.086 \pm 0.050$ | $2.7 \pm 4.2$ | $2.8 \pm 1.6$ | $0.2208 \pm 0.0053$ | −1991.64 |
| $z < 2.26$: 2067 quasars | $0.663 \pm 0.038$ | $-0.039 \pm 0.017$ | $6.2 \pm 1.2$ | $1.28 \pm 0.52$ | $0.2299 \pm 0.0038$ | −3903.08 |

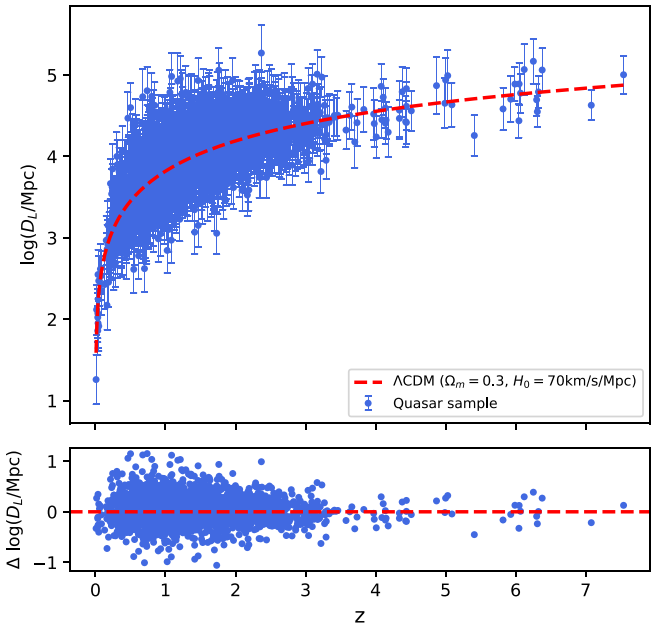


**Figure 3.** The constructed Hubble diagram of the calibrated quasar sample with median values of the quasar parameters. The upper plot shows the $\log(D_L)$–redshift relation for the 2421 calibrated quasars, and the red dashed line shows $\log(D_L)$ from the flat ΛCDM model with $\Omega_m = 0.3$ and $H_0 = 70$ km s$^{-1}$ Mpc$^{-1}$. The lower plot shows the residuals of $\log(D_L)$ obtained with best-fit quasar sample obtained assuming a flat ΛCDM model with $\Omega_m = 0.3$ and $H_0 = 70$ km s$^{-1}$ Mpc$^{-1}$.

alleviating the tension between the high-redshift and low-redshift quasar sample. However, with the increasing number of quasar calibration parameters to be fit, the uncertainties increase a lot for $\gamma$ and $\beta$. On the other hand, the results from 2067-quasar sample show good consistency with both the low-redshift quasar subsample and high-redshift quasar subsample, though of course with better precision. However, the uncertainties are still larger than the nonevolution of the quasar relation case. The resolution of the tension observed in quasar parameters may be attributed either to the evolution of the quasar calibration parameters or to host galaxy contamination.

Conversely, the low-redshift subsample is consistent with $\gamma_1 = 0$ and $\beta_1 = 0$, indicating no preference for evolution. However, the high-redshift subsample and the full sample prefer $\gamma_1$ and $\beta_1$ different than 0 at more than $3\sigma$. These results indicate that the preference for evolution in the quasar parameters is happening at high redshift and cannot be explained by a $z < 0.7$ cut and the corresponding host galaxy contamination.

### 3.3. Hubble Diagram of Quasars

Extrapolating the calibrated values of the quasar parameter sample and the intrinsic dispersion from the 2067 quasars to the full sample, which includes 2421 quasars, we can construct the Hubble diagram of quasars following

$$\log(D_L) = -\frac{1}{(2\gamma - 2)} \times [\gamma \log(F_{UV}) + (\gamma - 1)\log(4\pi) + \beta - \log(F_X)], \quad (5)$$

and the errors are obtained from error propagation considering the observed errors of $\log F_X$ and $\log F_{UV}$ as well as the intrinsic dispersion $\delta$. The results are shown in the upper plot of Figure 3. The red dashed line shows the $\log(D_L)$ from flat ΛCDM model with $\Omega_m = 0.3$ and $H_0 = 70$ km s$^{-1}$ Mpc$^{-1}$ following

$$D_L = \frac{c}{H_0}(1 + z) \int_z^z \frac{dz}{\sqrt{\Omega_m(1 + z)^3 + (1 - \Omega_m)}}. \quad (6)$$

We also calculate the residuals of $\log(D_L)$ obtained with the calibrated quasar sample obtained assuming a flat ΛCDM model with $\Omega_m = 0.3$ and $H_0 = 70$ km s$^{-1}$ Mpc$^{-1}$. The results are shown in the lower plot of Figure 3.

We can see the Hubble diagram is broadly consistent with the flat ΛCDM model. However, we will investigate in more detail the cosmological constraints with quasars as standard candles in a companion work.

**Table 4**
As Table 2 but for the Case where Quasar Parameters Do Evolve with Redshift as $\gamma(z) = \gamma_0 + \gamma_1 \times (1 + z)$ and $\beta(z) = \beta_0 + \beta_1 \times (1 + z)$

| Subsamples | $\gamma_0$ | $\gamma_1$ | $\beta_0$ | $\beta_1$ | $\delta$ | $\chi^2$ |
|---|---|---|---|---|---|---|
| $z < 1.16$: 1033 quasars | 0.657 | −0.019 | 6.33 | 0.63 | 0.2357 | −1919.35 |
| $z > 1.16$: 1034 quasars | 0.757 | −0.082 | 3.13 | 2.71 | 0.2204 | −2006.07 |
| $z < 2.26$: 2067 quasars | 0.671 | −0.043 | 6.08 | 1.46 | 0.2295 | −3908.27 |

## 4. Conclusions

Quasars are interesting potential standard candles since they would probe redshifts beyond those accessible by SNe Ia. However, there is a significant tension between the quasar calibration parameters if we consider the high-redshift quasars and low-redshift quasars separately. Therefore, we propose a case where the quasar calibration parameters evolve with redshift following $\gamma = \gamma_0 + \gamma_1(1 + z)$ and $\beta = \beta_0 + \beta_1(1 + z)$. The quasar sample is then calibrated in a cosmological-model-independent way by using the unanchored luminosity distances $D_L H_0$ reconstructed from the Pantheon+ SNe Ia data with GP regression.

Our results for the case where the quasar calibration parameters do not evolve with redshift show that there is about a $4\sigma$ tension between the quasar parameters $\gamma$ and $\beta$ when fitting the low-redshift quasar sample and the high-redshift quasar sample. In contrast, the case where the quasar calibration parameters are allowed to evolve with redshift, shows that the quasar calibration parameters are consistent at the $2\sigma$ level.

Although the uncertainties associated with the quasar calibration parameters increase due to the greater number of these parameters, the internal inconsistencies within the data are resolved. Further, the high-redshift and full samples prefer values of the extended parameters $\gamma_1$ and $\beta_1$ different than 0, indicating the restored consistency of the high-redshift and low-redshift subsamples is due to these evolution parameters and not simply due to increased uncertainties. While the tension between the high-redshift and low-redshift subsamples is mitigated by employing a conservative cut on quasars at redshift less than 0.7, the high-redshift subsample alone still prefers evolution in the quasar parameters. These considerations are detailed in the Appendix.

In conclusion, quasars could probe the Universe's expansion history at redshifts beyond those probed by SNe Ia if they can be calibrated accurately. We have shown that quasars are still sensitive probes of the Universe's expansion history, even allowing for more complicated but empirically driven extensions to the quasars' calibration relationship. This might, in principle, motivate some theoretical studies to discover a more accurate and physically motivated relationship for quasars' UV and X-ray luminosities. We hope future surveys with more accurate observations would be able to tell us if there is redshift evolution for the quasar UV and X-ray relationship and thus make the quasar sample a much more reliable cosmic probe.

## Acknowledgments

We thank Elisabeta Lusso for the valuable suggestions and comments. This work was supported by National Natural Science Foundation of China (NSFC) No. 12003006 and Science Research Project of Hebei Education Department No. BJK2024134. This work benefits from the high-performance computing clusters at College of Physics, Hebei Normal University. A.S. would like to acknowledge the support by National Research Foundation of Korea NRF2021M3F7A1082056 and the support of the Korea Institute for Advanced Study (KIAS) grant funded by the government of Korea.

## Appendix

After excluding quasars with a redshift below 0.7, the remaining sample comprises 1669 quasars exhibiting redshift range overlap with SNe Ia. This quasar sample is further stratified into two subsamples: a low-redshift group consisting of 834 quasars and a high-redshift group consisting of 835 quasars. Calibration is performed using $D_{\rm L}H_0$, reconstructed from SNe Ia utilizing GP, as outlined in Section 2. The results of this calibration are presented in Figure 4 and Table 5.

The findings indicate that the discrepancies between the low-redshift and high-redshift subsamples vanish, and the quasar parameters for these subsamples align within a $1\sigma$ statistical

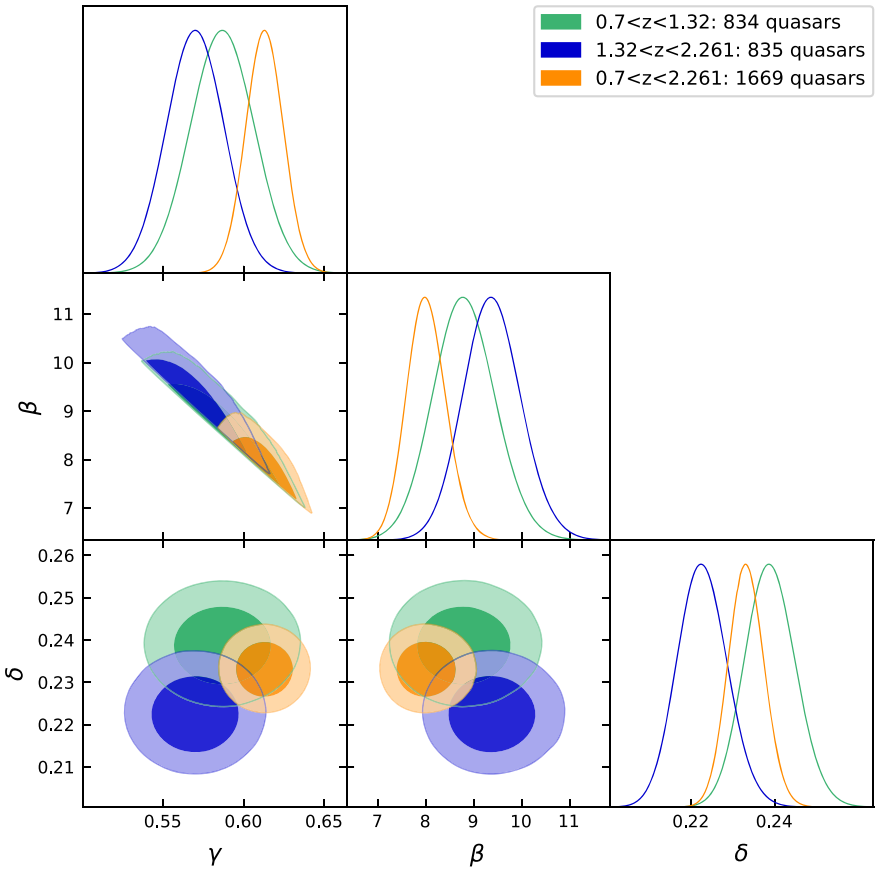


**Figure 4.** Calibration results for the quasar parameters with $z < 0.7$ quasars excluded for the case where they do not evolve with redshift.

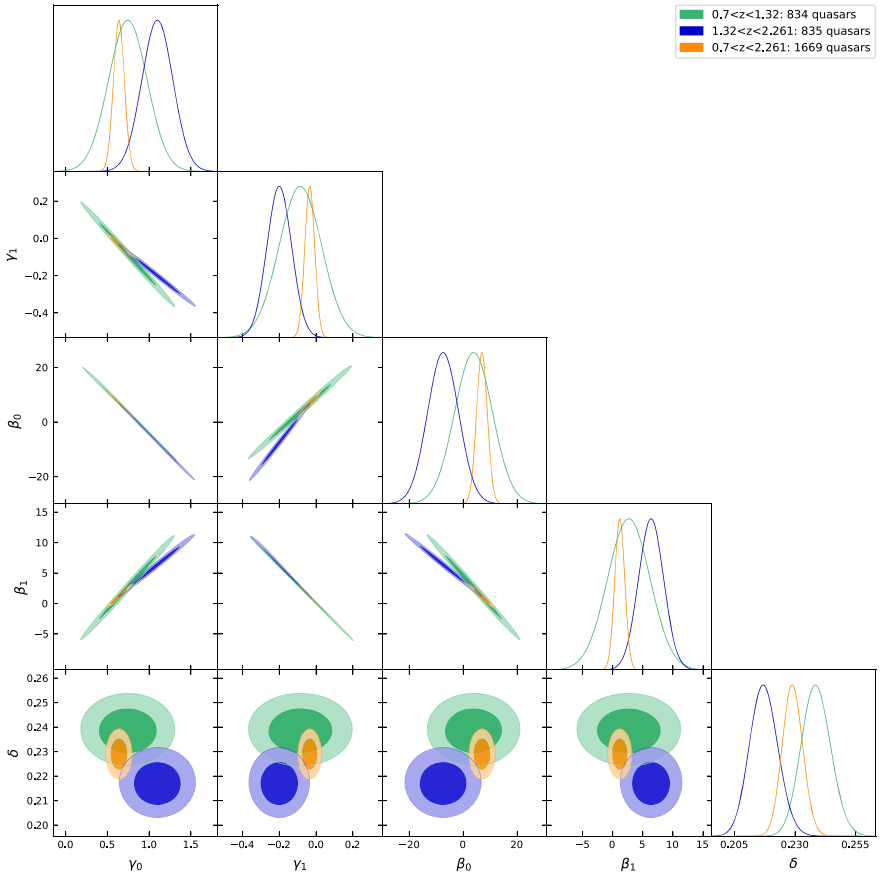


**Figure 5.** Calibration results for the quasar parameters with $z < 0.7$ quasars excluded for the case where they evolve with redshift.

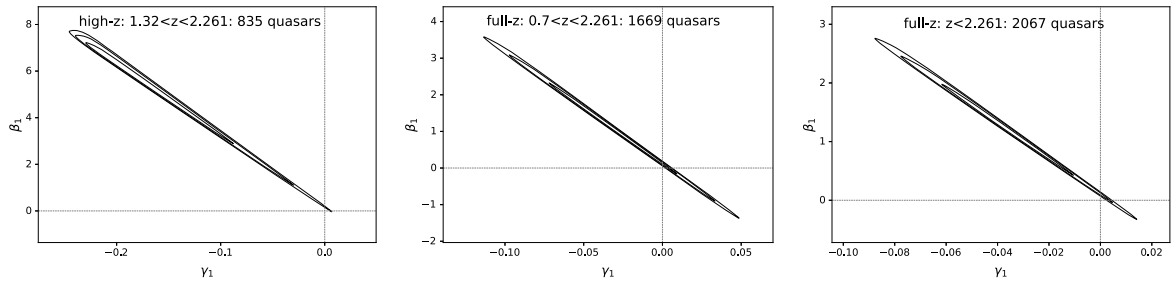


**Figure 6.** The posterior for the $\gamma_1$–$\beta_1$ relation in two-dimensional plots for the high-redshift quasar subsample (left panel), full quasar sample excluding $z < 0.7$ quasars (middle panel), and full quasar sample (right panel).

level of significance, but this can be due to rigidity of the functional form fitting the data (not being flexible enough). To validate this consistency, we allow then redshift evolution of the quasar parameters. The results are shown in Table 6 and Figure 5. We also show the two-dimensional contours for $\gamma_1$ and $\beta_1$ obtained with the high-z quasar subsample, the full quasar sample excluding $z < 0.7$ quasars, and the full quasar sample in Figure 6. We can see that zero slope ($\gamma_1 = 0$, $\beta_1 = 0$) is outside the $3\sigma$ contour for all the cases considered, which indicates that the quasar samples prefer a redshift evolution in the quasar calibration parameters regardless of any $z < 0.7$ contamination.

We further stratified the quasar sample with $z > 0.7$ into 13 redshift bins. Utilizing the mean values of 1000 GP reconstructed $D_L H_0$ realizations from SNe Ia, we systematically determined the quasar parameters ($\gamma$, $\beta$) across all bins. The bin-specific sample characteristics and calibration outcomes are comprehensively presented in Table 7 and Figure 7, with the latter demonstrating a distinct negative correlation for $\gamma$ and positive correlation for $\beta$ that aligns with the tabulated results.

**Table 5**
The Median Values of the Quasar Parameters and Their $1\sigma$ Uncertainties with $z < 0.7$ Quasars Excluded for the Case where They Do Not Evolve with Redshift

| Subsamples | $\gamma$ | $\beta$ | $\delta$ |
|---|---|---|---|
| $0.7 < z < 2.26$: 1669 quasars | $0.613 \pm 0.012$ | $8.01^{+0.38}_{-0.43}$ | $0.2332 \pm 0.0043$ |
| $0.7 < z < 1.32$: 834 quasars | $0.587 \pm 0.020$ | $8.80 \pm 0.65$ | $0.2389 \pm 0.0061$ |
| $1.32 < z < 2.26$: 835 quasars | $0.570 \pm 0.018$ | $9.38 \pm 0.60$ | $0.2227 \pm 0.0060$ |

**Note.** GP reconstructions of $D_L H_0$ based on the Pantheon+ SNe Ia compilation were used.

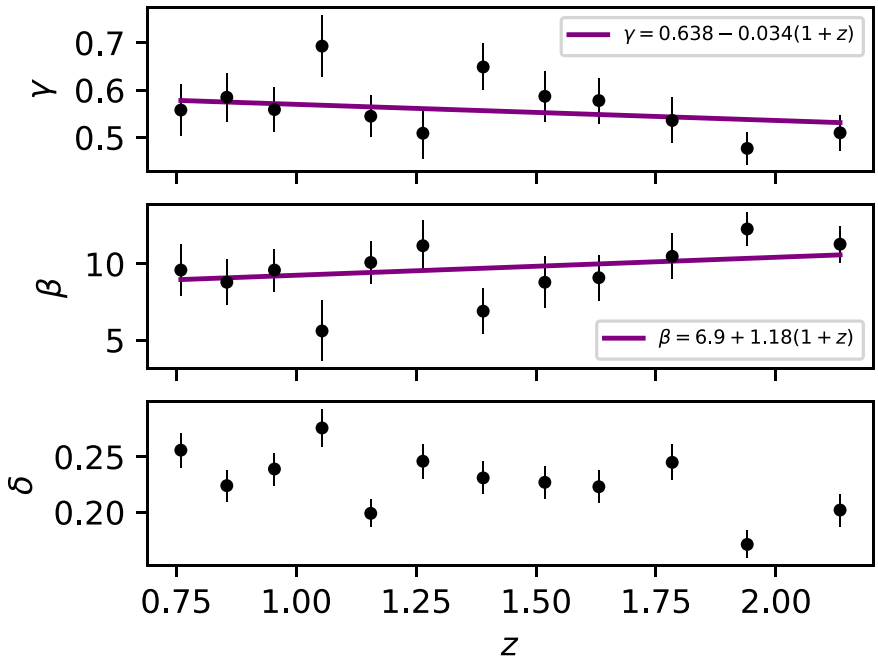


**Figure 7.** The constraint results for quasar parameters with each quasar bin.

**Table 6**
As Table 5 but for the Case where Quasar Parameters Do Evolve with Redshift as $\gamma(z) = \gamma_0 + \gamma_1 \times (1+z)$ and $\beta(z) = \beta_0 + \beta_1 \times (1+z)$

| Subsamples | $\gamma_0$ | $\gamma_1$ | $\beta_0$ | $\beta_1$ | $\delta$ |
|---|---|---|---|---|---|
| $0.7 < z < 2.26$: 1669 quasars | $0.638 \pm 0.065$ | $-0.034 \pm 0.027$ | $6.9 \pm 2.0$ | $1.18 \pm 0.83$ | $0.2290 \pm 0.0042$ |
| $0.7 < z < 1.32$: 834 quasars | $0.740 \pm 0.230$ | $-0.090 \pm 0.120$ | $3.8 \pm 7.0$ | $2.7 \pm 3.5$ | $0.2387 \pm 0.0061$ |
| $1.32 < z < 2.26$: 835 quasars | $1.100 \pm 0.190$ | $-0.200 \pm 0.067$ | $-7.5 \pm 5.8$ | $6.4 \pm 2.1$ | $0.2172 \pm 0.0058$ |

**Table 7**
The Detail of the Quasar Bins Including the Number of the Quasar, the Redshift Range, and the Mean Redshift for Each Quasar Bin

| Number of Quasars | $z$ | $z_{\rm mean}$ | $\gamma$ | $\beta$ |
|---|---|---|---|---|
| 138 | $0.712 < z < 0.805$ | 0.7596 | $0.558 \pm 0.054$ | $9.6 \pm 1.7$ |
| 138 | $0.805 < z < 0.906$ | 0.8554 | $0.585 \pm 0.051$ | $8.8 \pm 1.5$ |
| 138 | $0.9066 < z < 1.0005$ | 0.9547 | $0.559 \pm 0.047$ | $9.6 \pm 1.4$ |
| 138 | $1.0021 < z < 1.1099$ | 1.0539 | $0.693 \pm 0.065$ | $5.6 \pm 2.0$ |
| 138 | $1.1105 < z < 1.204$ | 1.1555 | $0.545 \pm 0.044$ | $10.1 \pm 1.4$ |
| 138 | $1.2046 < z < 1.3311$ | 1.2641 | $0.509 \pm 0.054$ | $11.2 \pm 1.7$ |
| 138 | $1.332 < z < 1.4569$ | 1.3898 | $0.649 \pm 0.049$ | $6.9 \pm 1.5$ |
| 138 | $1.4592 < z < 1.574$ | 1.5183 | $0.587 \pm 0.053$ | $8.8 \pm 1.7$ |
| 138 | $1.5751 < z < 1.703$ | 1.6309 | $0.578 \pm 0.048$ | $9.1 \pm 1.5$ |
| 138 | $1.703 < z < 1.869$ | 1.7838 | $0.536 \pm 0.048$ | $10.5 \pm 1.5$ |
| 138 | $1.87 < z < 2.0318$ | 1.9402 | $0.477 \pm 0.034$ | $12.3 \pm 1.1$ |
| 135 | $2.0336 < z < 2.261$ | 2.1337 | $0.510 \pm 0.038$ | $11.3 \pm 1.2$ |

**Note.** The last two columns give the constraint results from each quasar bin.

## ORCID iDs

Xiaolei Li https://orcid.org/0000-0002-2154-0394
Arman Shafieloo https://orcid.org/0000-0001-6815-0337

## References

Avni, Y., & Tananbaum, H. 1986, ApJ, 305, 83
Baldwin, J. A. 1977, ApJ, 214, 679
Banados, E., Venemans, B. P., Mazzucchelli , C., et al. 2018, Natur, 553, 473
Carroll, S. M., Press, W. H., & Turner, E. L. 1992, ARA&A, 30, 499
Di Valentino, E., Mena, O., Pan, S., et al. 2021, CQGra, 38, 153001
Dolgov, A. D. 1997, arXiv:astro-ph/9708045
Foreman-Mackey, D., Hogg, D. W., Lang, D., & Goodman, J. 2013, PASP, 125, 306
Holsclaw, T., Alam, U., Sanso, B., et al. 2010, PhRvD, 82, 103502
Holsclaw, T., Alam, U., Sansó, B., et al. 2011, PhRvD, 84, 083501
Hwang, S.-g., L'Huillier, B., Keeley, R. E., Jee, M. J., & Shafieloo, A. 2023, JCAP, 02, 014
Joudaki, S., Kaplinghat, M., Keeley, R., & Kirkby, D. 2018, PhRvD, 97, 123501
Khadka, N., & Ratra, B. 2020, MNRAS, 497, 263
Khadka, N., & Ratra, B. 2021, MNRAS, 502, 6140

Kilerci Eser, E., Vestergaard, M., Peterson, B. M., Denney, K. D., & Bentz, M. C. 2015, ApJ, 801, 8
La Franca, F., Bianchi, S., Ponti, G., Branchini, E., & Matt, G. 2014, ApJL, 787, L12
Lewis, A. 2019, arXiv:1910.13970
Li, X., Keeley, R. E., Shafieloo, A., et al. 2021, MNRAS, 507, 919
Li, Z., Huang, L., & Wang, J. 2022, MNRAS, 517, 1901
Liao, K., Shafieloo, A., Keeley, R. E., & Linder, E. V. 2019, ApJL, 886, L23
Liao, K., Shafieloo, A., Keeley, R. E., & Linder, E. V. 2020, ApJL, 895, L29
Lusso, E., Comastri, A., Vignali, C., et al. 2010, A&A, 512, A34
Lusso, E., & Risaliti, G. 2017, A&A, 602, A79
Lusso, E., et al. 2020, A&A, 642, A150
Martin, J. 2012, CRPhy, 13, 566
Melia, F. 2014, JCAP, 01, 027
Mortlock, D. J., Warren, S. J., Venemans, B. P., et al. 2011, Natur, 474, 616
Osmer, P. S., & Shields, J. C. 1999, in ASP Conf. Ser. 162, Quasars and Cosmology, ed. G. Ferland & J. Baldwin (San Francisco, CA: ASP), 235
Planck Collaboration, Aghanim, N., Akrami, Y., et al. 2020, A&A, 641, A6
Rasmussen, C. E., & Williams, C. K. I. 2006, Gaussian Processes for Machine Learning (Cambridge, MA: MIT Press)
Riess, A. G., Casertano, S., Yuan, W., Macri, L. M., & Scolnic, D. 2019, ApJ, 876, 85
Risaliti, G., & Lusso, E. 2015, ApJ, 815, 33
Risaliti, G., & Lusso, E. 2017, AN, 338, 329
Risaliti, G., & Lusso, E. 2019, NatAs, 3, 272
Sacchi, A., Risaliti, G., Signorini, M., et al. 2022, A&A, 663, L7
Scolnic, D., Brout, D., Carr, A., et al. 2022, ApJ, 938, 113
Shafieloo, A., Kim, A. G., & Linder, E. V. 2012, PhRvD, 85, 123530
Tananbaum, H., Avni, Y., Branduardi, G., et al. 1979, ApJL, 234, L9
Vagnetti, F., Turriziani, S., Trevese, D., & Antonucci, M. 2010, A&A, 519, A17
Wang, B., Liu, Y., Yu, H., & Wu, P. 2024, ApJ, 962, 103
Wang, B., Liu, Y., Yuan, Z., et al. 2022, ApJ, 940, 174
Wang, F., Yang, J., Fan, X., et al. 2021, ApJL, 907, L1
Wang, J. M., Du, P., Valls-Gabaud, D., Hu, C., & Netzer, H. 2013, PhRvL, 110, 081301
Watson, D., Denney, K. D., Vestergaard, M., & Davis, T. M. 2011, ApJ, 740, L49
Weinberg, S. 1989, RvMP, 61, 1
Zamorani, G., Henry, J. P., Maccacaro, T., et al. 1981, ApJ, 245, 357